Applied Physics A (2024) 130:879
https://doi.org/10.1007/s00339-024-08032-2

Applied Physics A
Materials Science & Processing

Structure, electrophysical, optical, and magnetic properties of composites (1-*x*)$PbFe_{12}O_{19}$–*x*$PbTiO_3$

Kamaludin Abdulvakhidov[1] · Nurzod Yunusov[2] · Salim Otajonov[2] · Ravshan Ergashev[2] · Zhengyou Li[1] · Bashir Abdulvakhidov[3] · Suleiman Kallaev[4] · Aram Manukyan[5] · Abeer Alshoekh[1] · Marina Sirota[1] · Alexander Soldatov[1] · Alexander Nazarenko[6] · Pavel Plyaka[6] · Elza Ubushaeva[7] · Harutyun Gyulasaryan[5]

Received: 7 August 2024 / Accepted: 27 October 2024 / Published online: 12 November 2024

Abstract

This paper presents the results of studying the structural features and physical properties of two-component composites (1-*x*)$PbFe_{12}O_{19}$–*x*$PbTiO_3$, obtained from pre-synthesized and mechanically activated powders. To control the physical properties of composites, in addition to changing the dopant ($PbTiO_3$) concentration within the range of 0.2–0.8 in steps of 0.2, the method of mechanical activation (nanostructuring) was used. This method implies that the Bridgman anvils simultaneously apply a compressive force to the powder placed between them and produce a shear deformation by rotating the lower anvil. X-ray diffraction revealed a sharp decrease in the unit cell parameters of the dopant of the initial composition at $x = 0.4$, followed by a similarly sharp leap in the parameters of the hexagonal cell after mechanical activation. The dimensions of the coherent scattering regions (D) of the $PbFe_{12}O_{19}$ component after mechanical activation decreased by more than a half, while the dislocation density (ρ_D) and the magnitude of microstrains (ε) increased by more than an order of magnitude. It was found that the magnetic phase transition temperature of composites decreases by about 14 °C with increasing dopant concentration, and the nanostructuring of composites leads to a further decrease in the transition temperature by another 12–36 °C, depending on the dopant concentration. The band gap E_g of the nanostructured compositions increases by approximately 0.3 eV regardless of the dopant concentration. Using the impedance spectroscopy method, it has been discovered that the dependence of the grain capacitance $C_g(T)$ in the temperature range of 150–350 °C has a bell-shaped form, which is explained in terms of Maxwell–Wagner polarization, where the relaxation is of the non-Debye type.

Keywords Composites · (1-*x*)$PbFe_{12}O_{19}$–*x*$PbTiO_3$ · Mechanical activation · Impedance spectroscopy · Band gap · FORC analysis

1 Introduction

The recent increased interest in M-type hexaferrites, commonly designated in the literature as $MFe_{12}O_{19}$ (M – Ba, Sr, Pb, etc.), is primarily due to the fact that they are important functional materials characterized by high values of saturation magnetization, magnetocrystalline anisotropy, coercivity, and resistance to external degrading factors [1]. M-type hexaferrites also belong to the class of multiferroic materials that exhibit both magnetic and charge ordering [2, 3], which makes them potential candidates for practical applications in various fields of science and technology [4–12]. Although the first characterized M-type hexaferrite is $PbFe_{12}O_{19}$, its magnetic properties are inferior to those of lead-free hexaferrites such as $BaFe_{12}O_{19}$ and $SrFe_{12}O_{19}$. Despite this fact and the gradual shift from the use of lead-containing

---

✉ Kamaludin Abdulvakhidov
phys.kam@mail.ru

[1] Southern Federal University, Sladkova 178/24, Rostov-on-Don, Russia 344090

[2] Fergana State University, Murabbiylar 19, 100150 Fergana, Uzbekistan

[3] Dagestan State University, Gadgieva 43a, Makhachkala, Russia 367000

[4] Dagestan Federal Research Centre of the Russian Academy of Sciences, Makhachkala, Russia 532096

[5] Institute for Physical Research, NAS of Armenia, 0204 Ashtarak, Armenia

[6] Southern Scientific Center of the Russian Academy of Sciences, Chekhova 41, Rostov-on-Don, Russia 344006

[7] Moscow Aviation Institute, Volokolamskoe Shosse 4, Moscow, Russia 125993

materials to lead-free materials in products and devices, the interest in studying $PbFe_{12}O_{19}$ remains high due to its easy synthesis [13–20].

To obtain hexaferrites and improve their physical properties, researchers employ various technological techniques and methods. In [21, 22] the authors describe co-precipitation, crystallization, hydrothermal, and microemulsion techniques, while in [23] the synthesis of nanostructures of $PbFe_{12}O_{19}$ was conducted with the citrate precursor method. However, this synthesis was accompanied by the formation of an impurity phase, γ-Fe_2O_3. In [24, 25], hexagonal structure $PbFe_{12}O_{19}$ powders were synthesized using the sol–gel method. In [24], ceramics sintered from these powders at room temperature exhibited significant spontaneous polarization, demonstrating a clear ferroelectric hysteresis loop with a residual polarization of $P_r \sim 33.5$ μC/cm^2. In [17], $PbFe_{12}O_{19}$ nanoparticles were obtained with a simple deposition method using various organic surfactants. Additionally, $PbFe_{12}O_{19}$-TiO_2 nanocomposites were prepared using the sol–gel method, and the influence of the deposition agent on the morphology and particle size, as well as the magnetic and photocatalytic properties of the composition were investigated. In [26], the changes in phase purity, morphology, and magnetic properties of $Ba_xPb_{1-x}Fe_{12}O_{19}$ ($x = 0$, 0.2, 0.4, 0.6, 0.8, and 1) hexaferrite powders synthesized by the sol–gel auto-combustion method were investigated depending on the annealing temperature (T_a). The hexagonal phase $PbFe_{12}O_{19}$ is formed directly as a result of the solid-state reaction between α-Fe_2O_3 and PbO during annealing of the combustion product at $T_a \sim 900$ °C.

The study [27] reports the synthesis of hexagonal ferrite $PbFe_{12}O_{19}$ by thermal decomposition of nitrates dissolved in ethylene glycol at 900 °C. The main advantages of this method, according to the authors, are the possibility of crystallization at low temperatures and the production of submicrometer particles.

A well-known method that leads to multiferroic properties in compositions is the synthesis of two-phase composites of hexaferrites and ferroelectrics, which are characterized by strong magnetoelectric interactions [13, 28–30].

Various methods of producing thin films also hold a significant place among the methods for obtaining hexaferrites. In the study [31], the thin polycrystalline $PbFe_{12}O_{19}$ films with high coercivity were grown on Si/SiO_2 substrates using pulsed laser ablation deposition. The influence of substrate temperature (550–775 °C) and oxygen pressure (1.0–3.0 mbar) on magnetic properties was observed. Crystallization of the thin $PbFe_{12}O_{19}$ films occurs in the temperature range of 600–750 °C, which is 100–150 °C lower than that of $SrFe_{12}O_{19}$ and $BaFe_{12}O_{19}$ hexaferrites. It was found that the films are isotropic with M_r/M_s, ratio of ~ 0.5, and the saturation magnetization of the films reaches 280 emu/cm^3, which is a fairly high value.

By using alternating targets of PbO and Fe_2O_3 with the laser ablation deposition method (ATLAD), the authors in [32] obtained oriented hexaferrite $PbFe_{12}O_{19}$. This configuration for film fabrication is notable because the properties of the film can be controlled by varying the target composition and the number of laser shots from each target during the deposition process. In another study [33], the thin $PbFe_{12}O_{19}$ hexaferrite films with a high degree of orientation in the perpendicular direction were fabricated by pulsed laser ablation on a sapphire substrate surface at 700 °C and the oxygen partial pressure of 3.0 mbar. The anisotropic nature of the films was demonstrated by the residual magnetization ratio $M_r/M_s = 86\%$ in the perpendicular direction compared to 20% in the direction parallel to the film plane. The coercive field value was 2.5 kOe and the saturation magnetization was 165 emu/cm^3.

Thus, from the small number of literature sources cited above, it is clear that the study of the same multiferroic property of $PbFe_{12}O_{19}$ yields varying results, and these depend on the technological methods and fabrication techniques used.

The aim of this study was to investigate the structural, optical, impedance, and magnetic properties of ceramic composites (1-x)$PbFe_{12}O_{19}$–$x$$PbTiO_3$, synthesized by the solid-state method, and to establish a "structure–property" correlation between compositions at the nanostructural and macroscopic scales. The selection of $PbTiO_3$ as the second component is due to its Curie temperature ($\sim T_c = 490$ °C), which is close to the magnetic phase transition temperature of $PbFe_{12}O_{19}$, reported to be around 430 °C [34]. This proximity of ferroelectric and magnetic phase transition temperatures is significant for the indirect control of the properties of the composite components.

2 Experimental procedures

2.1 Preparation of hexaferrite $PbFe_{12}O_{19}$

The starting oxides, PbO (≥ 99.9%, particle size < 10 μm) and Fe_2O_3 (≥ 99.9%, particle size < 5 μm) from Sigma-Aldrich, were mixed in stoichiometric proportions in an agate mortar for 2 h with ethanol as a medium. The mixture was then synthesized in a high-temperature furnace at 1250 °C for 2 h in an air atmosphere. The heating rate was 600 °C/h, and the cooling to room temperature took 10 h. The resulting product was ground for 30 min and analyzed for phase purity using an X-ray diffractometer (D2 Phaser, Bruker, Germany) with Cu Kα radiation ($K\alpha_1 = 1.54060$ Å, $K\alpha_2 = 1.54443$ Å), at a step size of $\Delta 2\theta = 0.01°$ and a data collection time $\tau = 0.1$ c. No impurity phases were detected.

2.2 Preparation of lead titanate $PbTiO_3$

Lead titanate $PbTiO_3$ was also synthesized using the solid-state reaction method. TiO_2 ($TiO_2 \geq 99.9\%$, particle size < 150 nm) and PbO (≥ 99.9%, particle size < 10 µm) from Sigma-Aldrich were mixed in stoichiometric proportions in an agate mortar with ethanol for 2 h. The synthesis was performed in a high-temperature furnace within a closed platinum crucible at 900 °C for 2 h in an air atmosphere. The heating rate was 300 °C/h, and the cooling to room temperature took 8 h. The resulting $PbTiO_3$ powder was ground in an agate mortar with ethanol along with the appropriate amount of $PbFe_{12}O_{19}$ for 2 h. A joint synthesis of $PbFe_{12}O_{19}$ and $PbTiO_3$ was then conducted at 900 °C for 4 h in an air atmosphere, followed by cooling to room temperature over 6 h.

2.3 Nanostructuring and characterization

For nanostructuring the pre-synthesized powder of $(1\text{-}x)PbFe_{12}O_{19}$–$xPbTiO_3$, the Bridgman anvils were employed as previously described in our works [35–37]. This method involves applying simultaneous compressive force using the Bridgman anvils to the powder placed between them, coupled with a shear deformation created by the rotation of the bottom anvil to introduce structural defects. For ceramic sintering, compressed tablets with a diameter of 11 mm were held in a furnace at 1100 °C for 2 h. For electrophysical studies, colloidal silver paste was applied to the ceramic disks and fired in a furnace for 15 min at 750 °C. Optical absorption spectra at room temperature were studied on a Shimadzu UV-2600 dual-beam spectrophotometer. Magnetic hysteresis loops were analyzed using a vibrating sample magnetometer (VSM, LakeShore 7404, USA) at room temperature. A high-temperature attachment was used to investigate the temperature dependence of magnetization. Impedance spectroscopy was studied using a PARSTAT 4000 impedance analyzer (Princeton Applied Research, USA) at high temperatures. Scanning electron micrographs were obtained using a microscope (Carl Zeiss EVO 40, Germany).

3 Results and discussion

3.1 Microstructure

Before nanostructuring, the samples exhibit well-defined crystallite facets corresponding to both the hexaferrite $PbFe_{12}O_{19}$ and the ferroelectric $PbTiO_3$. Depending on the concentration of x, the compositions show a range of grain sizes within certain intervals, which is presented as a histogram in the Supplementary Materials. After the mechanical activation, all samples exhibit a loose surface consisting of a collection of small, agglomerated nanoparticles (see Fig. 1). This agglomeration is due to the direct piezoelectric effect that occurs when pressure is applied to the macroscopic crystallites and leads to their crushes.

3.2 X-ray diffraction analysis

X-ray diffraction patterns of ceramic samples before and after nanostructuring are shown in Fig. 2(a), while the concentration dependence of the lattice parameters for the tetragonal and hexagonal phases of the composites is presented in Fig. 3. The refinement of the lattice parameters of the composite components was performed using the Rietveld method with the Powder Cell 2.3 software package [38]. The diffraction patterns are characterized by the broadening of Bragg profiles and their shift along the 2θ axis (see Fig. 2(b)). This is particularly noticeable for nanostructured compositions. $PbTiO_3$ has a tetragonal crystal system with the space group symmetry *P4mm* (ICSD Collection Code 1610), while $PbFe_{12}O_{19}$ has a hexagonal crystal system with the space group symmetry $P6_3/mmc$ (ICSD Collection Code 16,156). After nanostructuring, the symmetry of the composite components was preserved.

With changing x, the lattice parameter a of $PbTiO_3$ slightly decreases, while the parameter c increases at $x = 0.4$ (see Fig. 3(a)). At this point, a sharp decrease in a^* and c^* is observed, followed by some minor changes as x increases further. The situation is different for the hexagonal component of the composite. Here, a sharp leap in the lattice parameters a and c is observed at $x = 0.2$. The mechanical activation of the composite at the pressure of 1 GPa does not lead to any significant changes in the hexagonal lattice parameters a^* and c^* (see Fig. 3(b)), and their changes with increasing concentration x are non-monotonic. This indicates that the structural sensitivity of $PbFe_{12}O_{19}$ is strong at $x = 0.2$, while the sensitivity to topological defects of the ferroelectric component of the composite is more pronounced at $x = 0.4$.

However, at different mechanical activation pressures, a high sensitivity to topological defects at different concentrations may be revealed, since mechanical activation is accompanied by ballistic diffusion processes leading to the absorption of "weaker grains" (more defective) by less defective "healthy grains." The predominance of the concentration of point defects over the concentration of linear defects also depends on the pressure of mechanical activation.

Shifts of some diffraction peaks can be attributed to various types of structural defects, such as interstitial defects, vacancies, etc. These defects are characteristic of the planes with certain Miller indices and depend on the type of a crystal lattice [39]. During mechanical activation, the number of such defects increases.

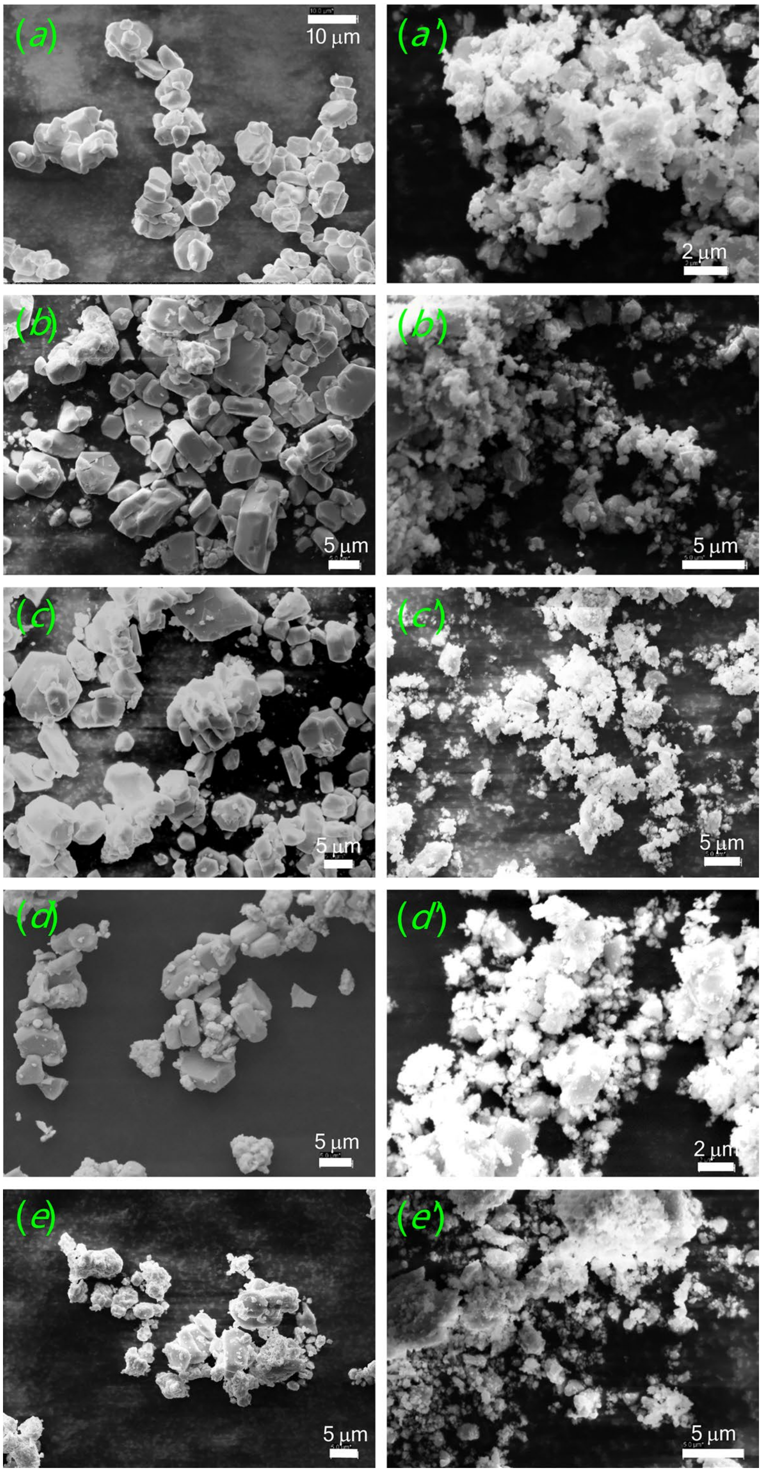

Fig. 1 SEM images of the powder samples, illustrating that the crystallites differ in morphology and habit before (left) and after (right) nanostructuring. (**a**), (*a′*) – $PbFe_{12}O_{19}$; (**b**), (*b′*) – $0.8PbFe_{12}O_{19}$-$0.2PbTiO_3$; (**c**), (*c′*) – $0.6PbFe_{12}O_{19}$-$0.4PbTiO_3$; (**d**), (*d′*) – $0.4PbFe_{12}O_{19}$-$0.6PbTiO_3$; (**e**), (*e′*) – $0.2PbFe_{12}O_{19}$-$0.8PbTiO_3$

Figure 4 shows the concentration dependences of the sizes of the coherent scattering regions (D) of the composite components.

To estimate the D value, we selected the non-overlapping peaks (114) of $PbFe_{12}O_{19}$ and (001) of $PbTiO_3$. The calculation was performed using the classical Debye–Scherrer formula:

$$D = (k \cdot \lambda)/(\beta \cos \theta) \tag{1}$$

where k is the dimensionless particle shape coefficient (Scherrer constant = 0.94); λ is the wavelength of the X-rays; β is the full width at half maximum (FWHM) of the reflection in radians; and θ is the diffraction angle (Bragg angle).

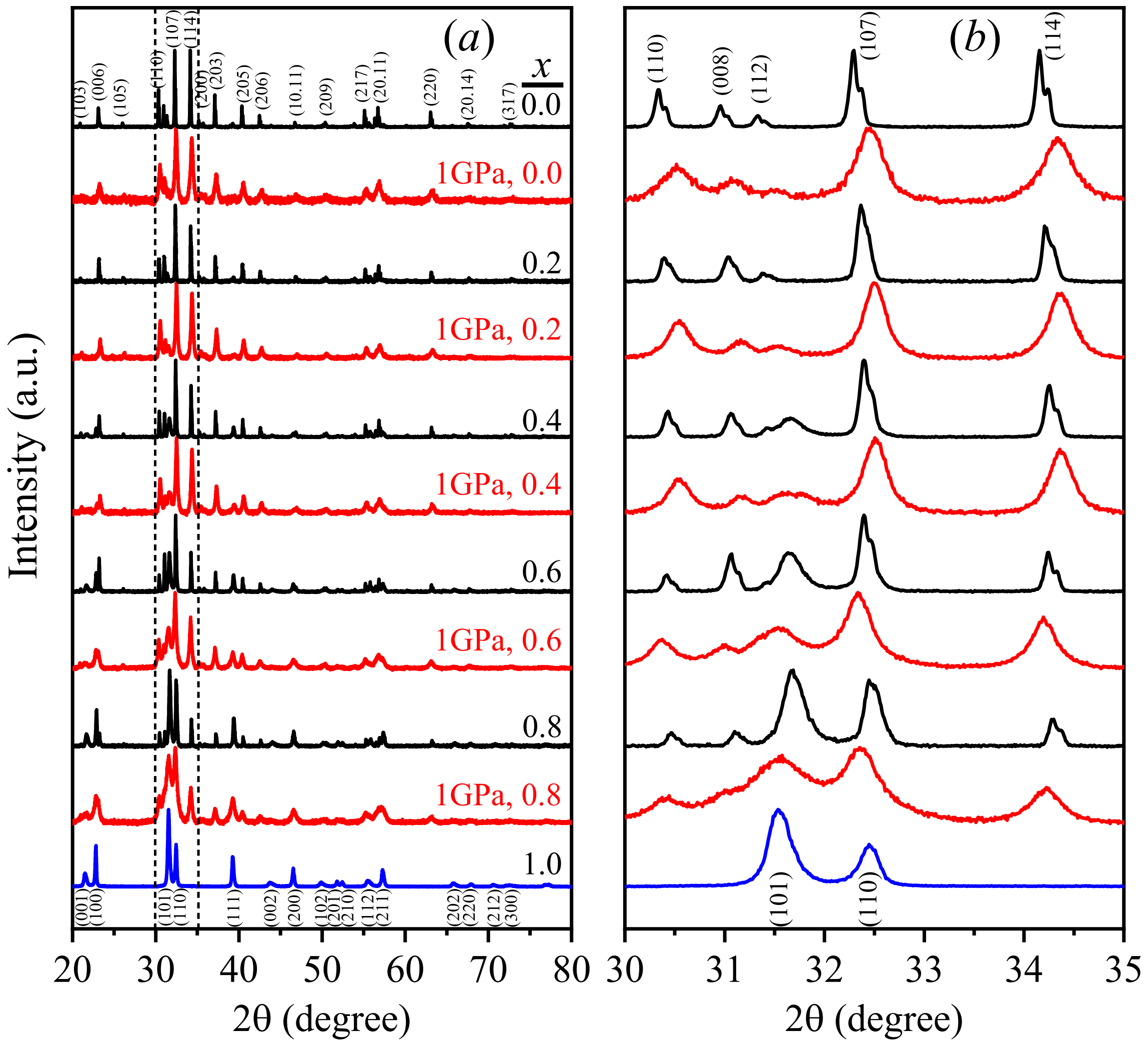

Fig. 2 X-ray diffraction patterns of initial and nanostructured composites (1-x)$PbFe_{12}O_{19}$–$x$$PbTiO_3$ (**a**) and selected angular interval (**b**)

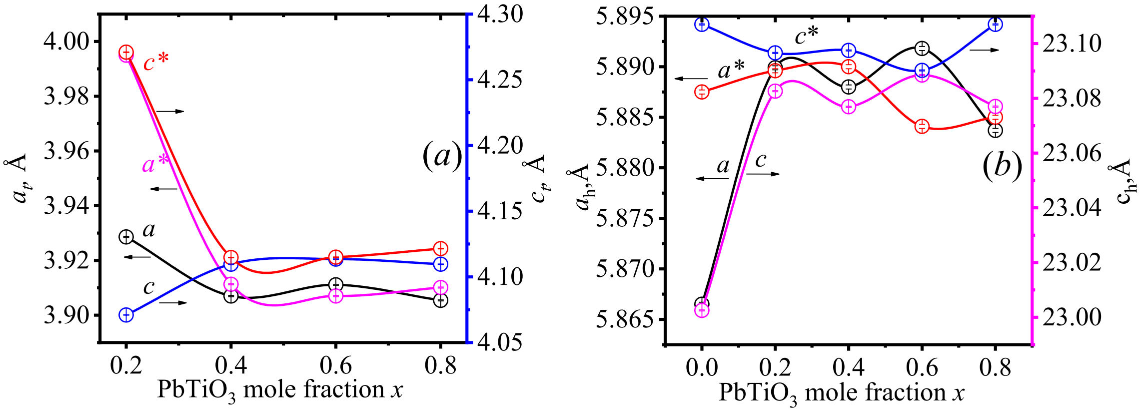

Fig. 3 Concentration dependence of the lattice parameters of the composite components $PbTiO_3$ (**a**) and $PbFe_{12}O_{19}$ (**b**) before and after nanostructuring at the pressure of 1 GPa. The graphs of the nanostructured compositions are indicated by an asterisk (*)

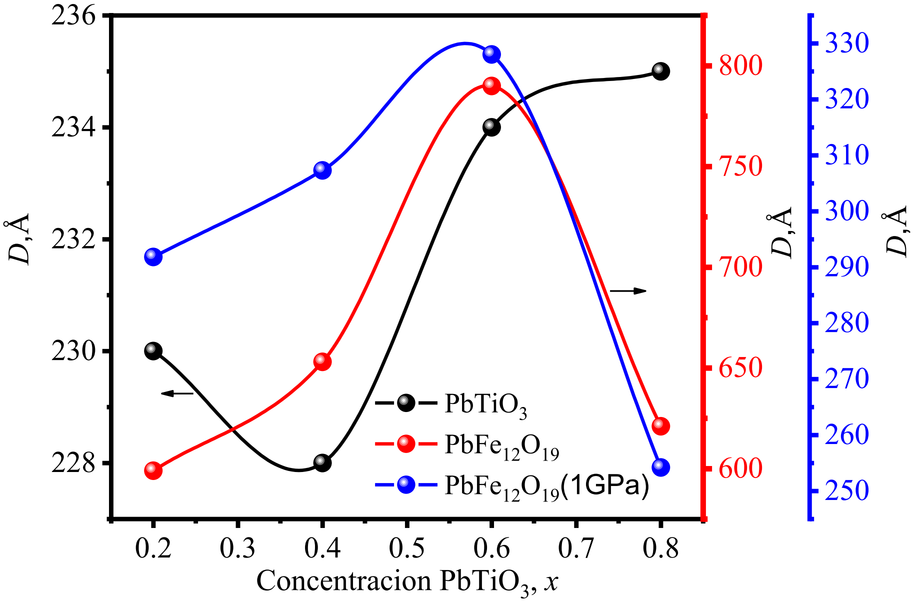

Fig. 4 Dependencies of D of the composite components on the concentration x and the pressure of mechanical activation

Table 1 Dislocation density (ρ_D) and microstrain (ε) values for (1-x) PbFe$_{12}$O$_{19}$ – xPbTiO$_3$

x	0.2	0.4	0.6	0.8
$\rho_D \times 10^{15}$/m^2 (PTO)	5.67	5.77	5.48	5.43
$\varepsilon \times 10^{-3}$	1.5	1.5	1.5	1.5
$\rho_D \times 10^{14}$ /m^2 (PFO)	8.36	7.04	4.81	7.78
$\varepsilon \times 10^{-4}$	5.9	5.4	4.5	5.7
$\rho_D \times 10^{15}$/m^2 (PFO) 1GPa	3.52	3.17	2.79	4.64
$\varepsilon \times 10^{-3}$-1GPa	1.1	1.1	1.4	1.0

From the figure, it can be seen that D of both components depends on the concentration x, with D of PbTiO$_3$ having a minimum value at $x = 0.4$. The behavior of D for PbFe$_{12}$O$_{19}$ before and after mechanical activation is similar; however, after mechanical activation, this value decreases by more than a half. Due to the weak intensities and blurring of reflection peaks from planes with Miller indices (001), the D value of PbTiO$_3$ after mechanical activation could not be reliably measured, so these values are not given here. Based on the experimental D data, the dislocation density for four concentrations was calculated (see Table 1) using the formula:

$$\rho D = 3nD^{-2} \tag{2}$$

with $n = 1$, assuming that the three-dimensional dislocation network coincides with the grain boundaries [40]. Microstrains were calculated using the formula:

$$\varepsilon = (\beta \cos \theta)/4 \tag{3}$$

where β is the FWHM.

As it is seen in the table, the dislocation density of PbFe$_{12}$O$_{19}$ and the microstrain values increase by more than an order of magnitude after mechanical activation.

3.3 Ferromagnetic properties

Integral parameters obtained from magnetic hysteresis loops in the presence of two or more phases with different magnetic states do not provide complete and reliable information about the magnetic domain structure, particle sizes, and interactions between them. The interpretation of the true magnetic state is also complicated in complex compositions—composites with more than one additional non-magnetic phase, where the spatial distribution of such phases can be random. Some additional difficulties in interpretation are also caused by the presence of topological defects introduced artificially in magnetic structures, as in our case.

Figure 5 shows the integral hysteresis loops before and after nanostructuring (see Fig. 5(a) and Fig. 5(b)), along with the corresponding parameters calculated from them. To calculate M_s for all concentrations, we constructed the dependencies $M(1/H^2)$ and extrapolated them to the intersection with the magnetization axis M (see Fig. 5(c) and Fig. 5(d)) to obtain the corresponding values.

The dependencies of the coercive field H_c and remanent magnetization M_r on the concentration x of the starting and nanostructured compositions, as well as the spontaneous magnetization M_s and the squareness ratio M_r/M_s, are presented in Fig. 5(e) and Fig. 5(f), respectively. As can be seen from the figures, they exhibit non-monotonic behavior, which is attributed to the domain structure and the inhomogeneous distribution of magnetization and local anisotropy in the samples.

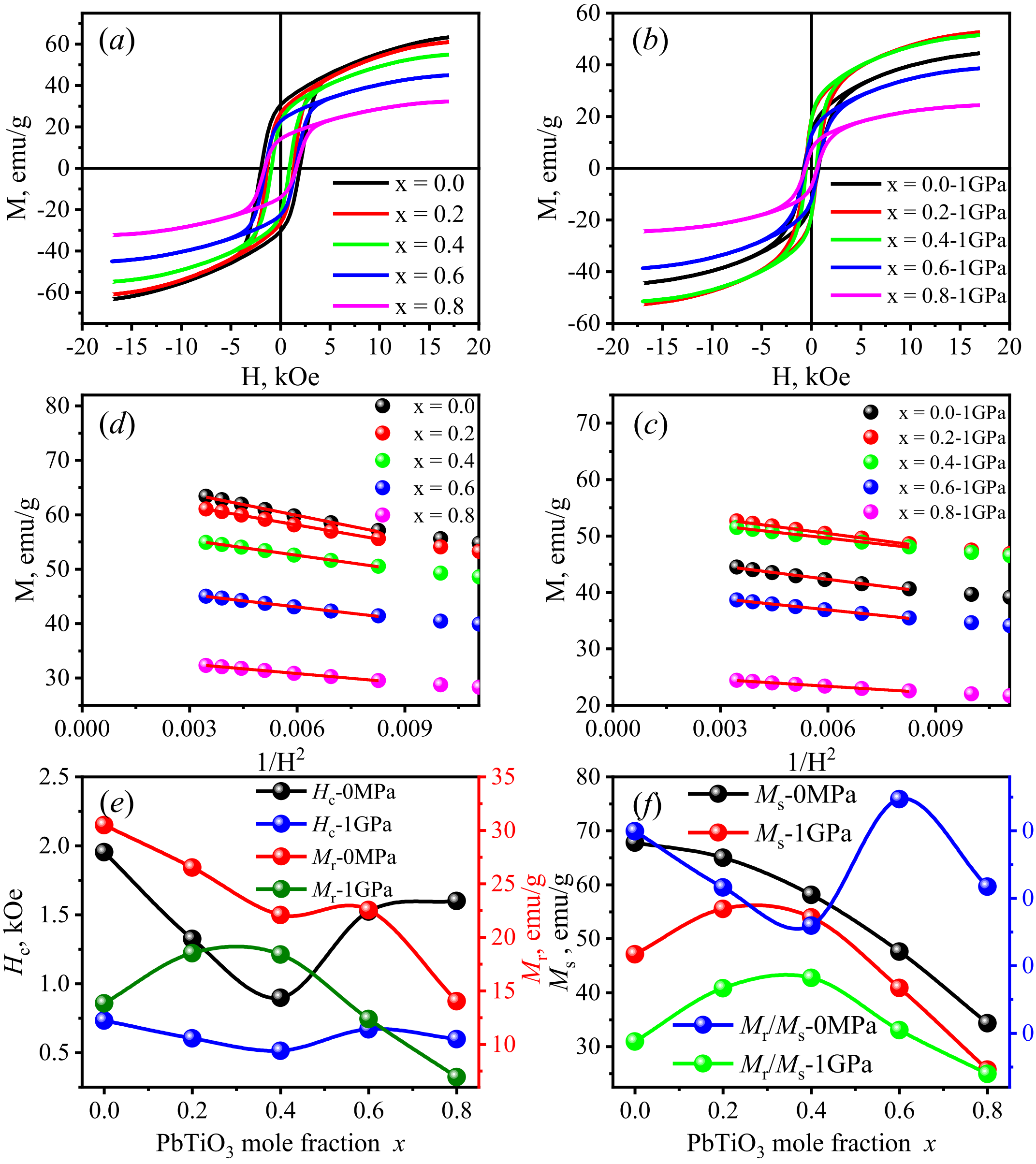

Fig. 5 Concentration dependence of the magnetic parameters of the composites before and after nanostructuring at the pressure of 1 GPa

However, many questions arising from the interpretation of results can be addressed using the FORC analysis (First Order Reversal Curves), which is based on measuring partial hysteresis loops [41].

Typically, at the beginning of the FORC diagram measurement, the sample is brought to magnetic saturation H_s. The next step is to reduce the field to H_a and then increase it until saturation due to the steps of the H_b field. This process is repeated multiple times for various H_a values. In our case, we performed 100 cycles. The FORC distribution is defined as:

$$\rho(H_a, H_b) = -\frac{\partial^2 M(H_a, H_b)}{\partial H_a \partial H_b} \qquad (4)$$

where $M(H_a, H_b)$ is the magnetization measured at the point (H_a, H_b).

In Fig. 6(a), this point is marked with a red cross.

Next, we transition from coordinates H_a and H_b to $H_c = (H_b - H_a)/2$ and $H_u = (H_b + H_a)/2$. However, it is not always possible to achieve magnetization saturation using commonly available laboratory magnetometers, and in

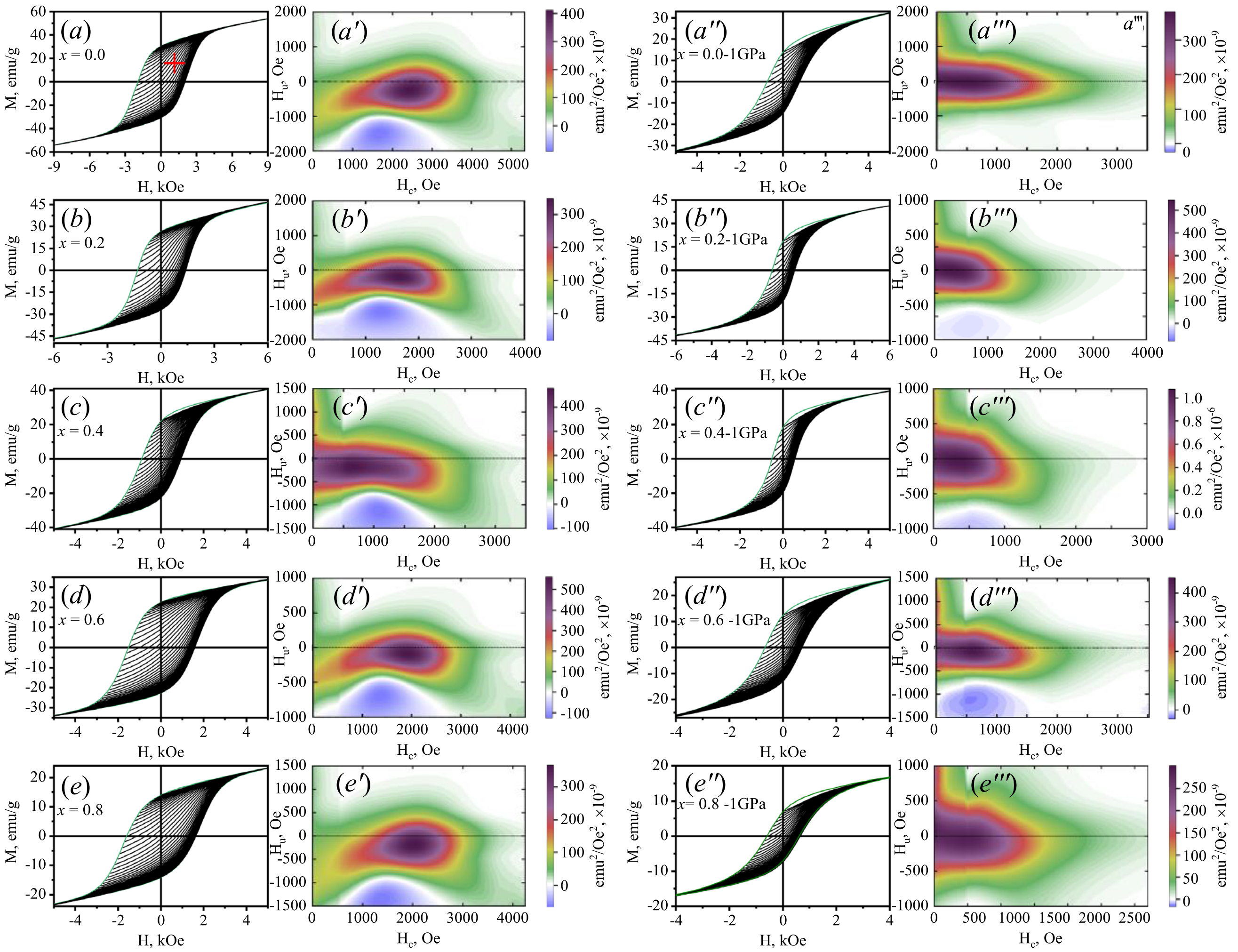

Fig. 6 A series of the FORC diagrams and two-dimensional representations of the distribution of coercive field and interaction field for the composites (1-x)$PbFe_{12}O_{19}$ – $x$$PbTiO_3$ before and after mechanical activation

such cases, the FORC analysis deals with unsaturated partial hysteresis loops. Figure 6(a', a''', b', b''', c', c''', d', d''', e', e''') shows the FORC diagrams and two-dimensional representations of the distribution of the coercive field and the interaction field for five concentrations of (1-x) $PbFe_{12}O_{19}$–$x$$PbTiO_3$. The measurement results were processed using the VARIFORC program [42].

As seen in Figs. 6(a, b, d, e), with increasing $PbTiO_3$ concentration, the areas of the FORC diagrams and the coercive field H_c, change non-monotonically. An exception is the concentration $x = 0.4$ (see Fig. 6(c)) which is characterized by a minimum value of H_c. The two-dimensional plots of the coercive field and interaction field distribution are shown in Figs. 6(a', b', c', d', e'), and, except for the concentration $x = 0.4$, they represent diagrams of single-domain non-interacting particles with ridges shifted downward along the interaction field axis H_u. The diagram for $x = 0.4$ corresponds to a multi-domain structure.

Nanostructuring of the compositions, except for the composition with $x = 0.8$, resulted in the narrower FORC diagrams (see Fig. 6(a'', b'', c'', d'', e'')), and the two-dimensional images are similar to the diagrams of multi-domain structures. It should be noted that during nanostructuring by mechanical activation, in addition to the saturation of the compositions with structural defects, there is also particle dispersion.

The spread of particle sizes during mechanical activation is multimodal in its nature, and the H_c values of the magnetized regions vary accordingly. The influence of stresses and grain size on the hysteresis parameters and the ambiguity of their results were indicated earlier in [43, 44].

3.4 Temperature dependence of magnetization

The stability of the structure and magnetic properties under various external influences are crucial factors determining the practical applicability of functional materials. It was of interest to study the behavior of the magnetization M of the composites (1-x)$PbFe_{12}O_{19}$–$x$$PbTiO_3$ at high temperatures and to clarify the role of the dopant and structural defects during the magnetic phase transition of the composites.

Figure 7 shows the temperature dependence of the magnetization for five concentrations of the initial compositions and the compositions after mechanical activation. As seen in Fig. 7(a), the magnetic phase transition of $PbFe_{12}O_{19}$ starts at about 623 K (350 °C) and completes at $T = 683$ K (410 °C), which is 20 K lower than the Néel temperature T_N found in [34]. For clarity, the regions marking the start and completion of the magnetic phase transition are indicated by ellipses in Fig. 6.

As the concentration x increases, the temperatures at which the phase transition starts and finishes shift downward. Despite the fact that the coercive force of the composites increases with higher x concentrations, except for $x = 0.4$, the temperatures at which phase transitions start and finish shift to the left.

For nanostructured compositions, the coercive force H_c decreases (see Fig. 6(a'', b'', c'', d'', e'')), the phase transitions start and finish at lower temperatures (see Fig. 7(a')), and the $M(T)$ dependencies exhibit a more gradual slope. These compositions also have lower magnetization values. Here, the particle sizes and their structural state play a significant role, as they are smaller and more defective compared to the initial compositions.

3.5 Optical properties

Many fundamental parameters of solids, including the band gap E_g, are structurally sensitive. Therefore, it was of interest to study the influence of structural defects on the E_g of the composites (1-x)$PbFe_{12}O_{19}$–$x$$PbTiO_3$. Based on the diffuse reflectance $R(\lambda)$, we obtained absorption spectra. For their analysis, the Kubelka–Munk function, which is proportional to the ratio of the absorption coefficient α and the scattering coefficient s of an infinitely thick opaque sample, was used [45].

$$F(R) = (1-R)^2/2R = \alpha/s \tag{5}$$

To estimate the band gap, we used the equation proposed by Tauc, Davis, and Mott [46–49]:

$$(h\nu\,\alpha)^{1/n} = A\left(h\nu - E_g\right) \tag{6}$$

where h is the Planck's constant, ν is the frequency, and A is the proportionality coefficient, $n = 1/2$ for allowed direct transitions and $n = 2$ for allowed indirect transitions. The graphs of the dependence of $(E{\cdot}F(R_\infty))^2$ on $h\nu$ using the Kubelka–Munk function $(h\nu{\cdot}F(R_\infty))^2$ for the compositions are shown in Fig. 8. The tangent drawn to the intersection with the energy axis gives E_g. As can be seen from the Fig. 8, the E_g of all concentrations after the mechanical activation increased significantly. By changing the band gap in this way, we can control the charge transport properties of the compositions.

3.6 Impedance spectroscopy

Impedance spectroscopy, one of the relaxation methods, has been used to analyze the parameter behavior of nonlinear elements in electrical circuits of crystalline bodies. The nonlinear elements of the electrical circuit, which include the samples studied in this work, are nonlinear capacitors. In this

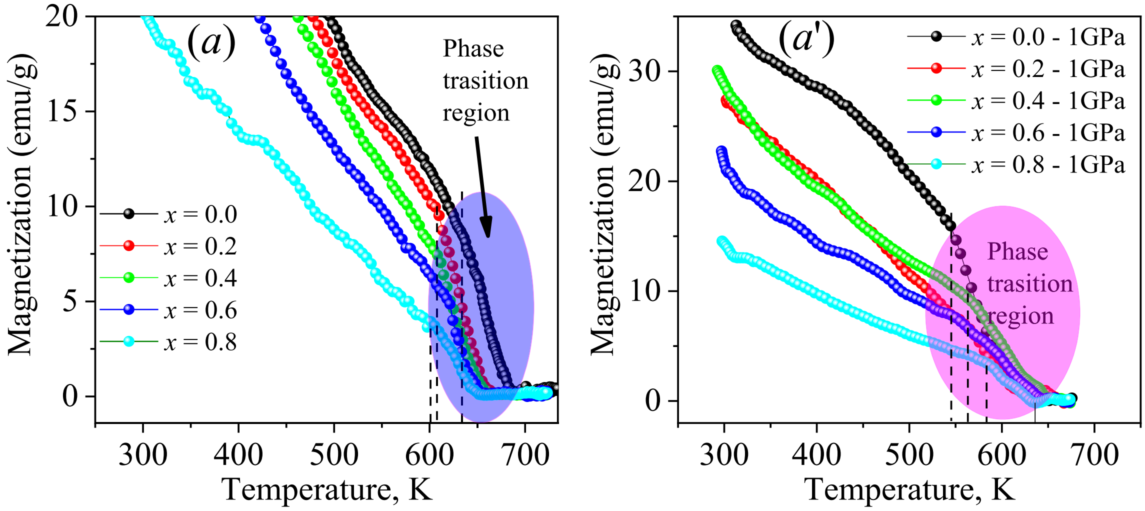

Fig. 7 Temperature dependencies of the magnetization of (1-x)$PbFe_{12}O_{19}$ – $x$$PbTiO_3$ before (**a**) and after (**a′**) nanostructuring. The ellipsoids correspond to the start and completion of phase transitions

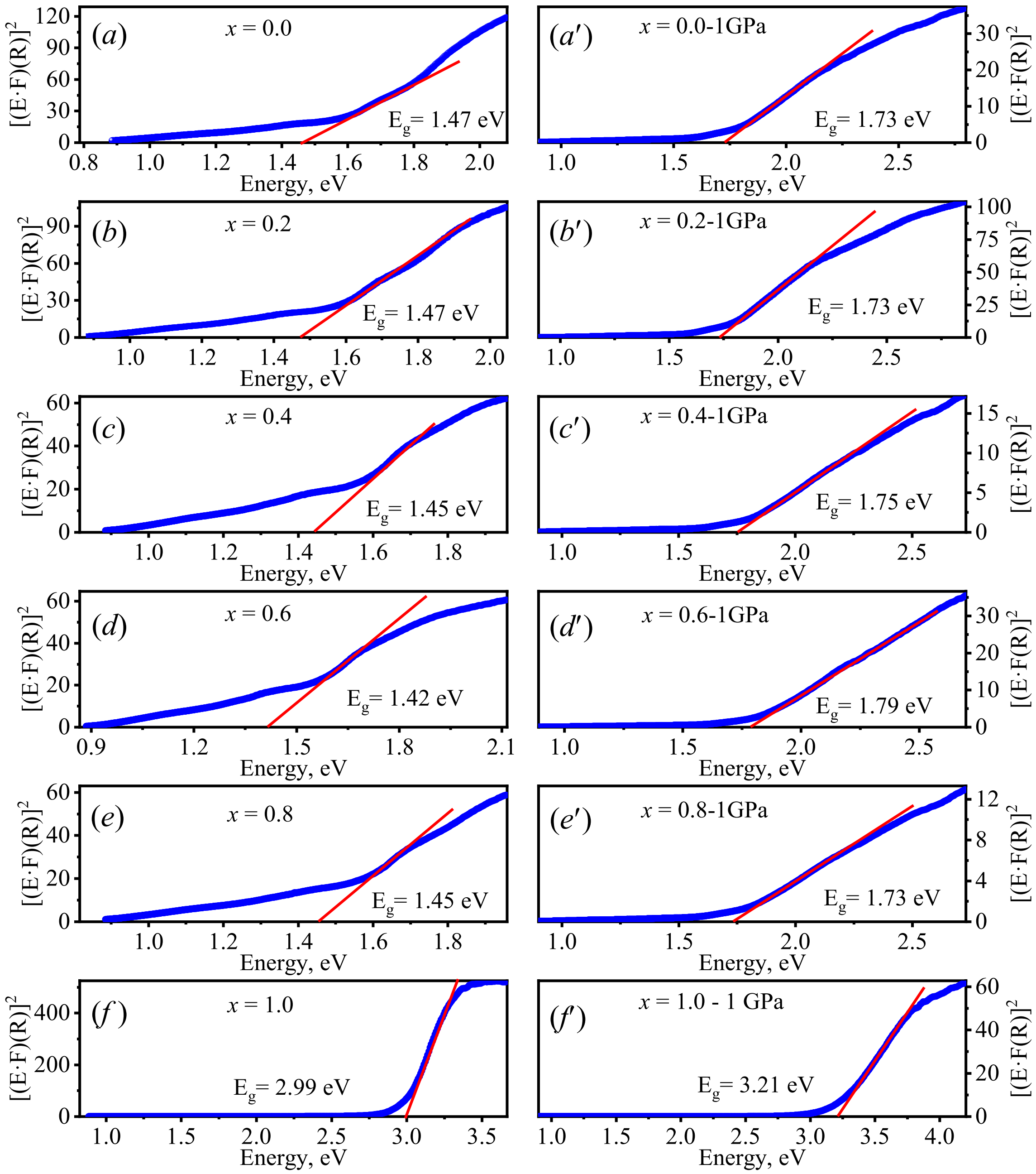

Fig. 8 Dependence of the function $(E{\cdot}F(R_\infty))^2$ on the energy E of the initial (**a**, **b**, **c**, **d**, **e**, **f**) and mechanically activated (**a′**, **b′**, **c′**, **d′**, **e′**, **f′**) samples $(1\text{-}x)\mathrm{PbFe_{12}O_{19}} - x\mathrm{PbTiO_3}$

case, the controlled parameters are the capacitances C_{gb}, C_g as well as the resistances R_{gb} and R_g of the grain boundaries and grain volumes of the samples, which determine the charge transport properties of the materials.

Figure 9 shows the frequency dependencies of the real and imaginary parts of the complex impedance Z^* and the Cole–Cole plots $Z''(Z')$ for various temperatures. The $Z'(\omega)$ dependencies of all compositions show three distinct regions: the first region is frequency-independent and depends only on temperature; the second region depends on both frequency and temperature; and the third region begins at the point where all lines merge into a straight line (see Fig. 9(*a*, *b*, *c*, *d*, *e*)). To the right of this point, the charge transport properties are mainly due to the constant component of electrical conductivity. Note that this division of the $Z'(\omega)$ dependence into regions is conditional, and the boundaries of these regions depend on both the concentration x and the density of topological defects.

In Fig. 9(*a′*, *b′*, *c′*, *d′*, *e′*), the $Z''(\omega)$ dependencies are shown representing bell-shaped and slightly asymmetric

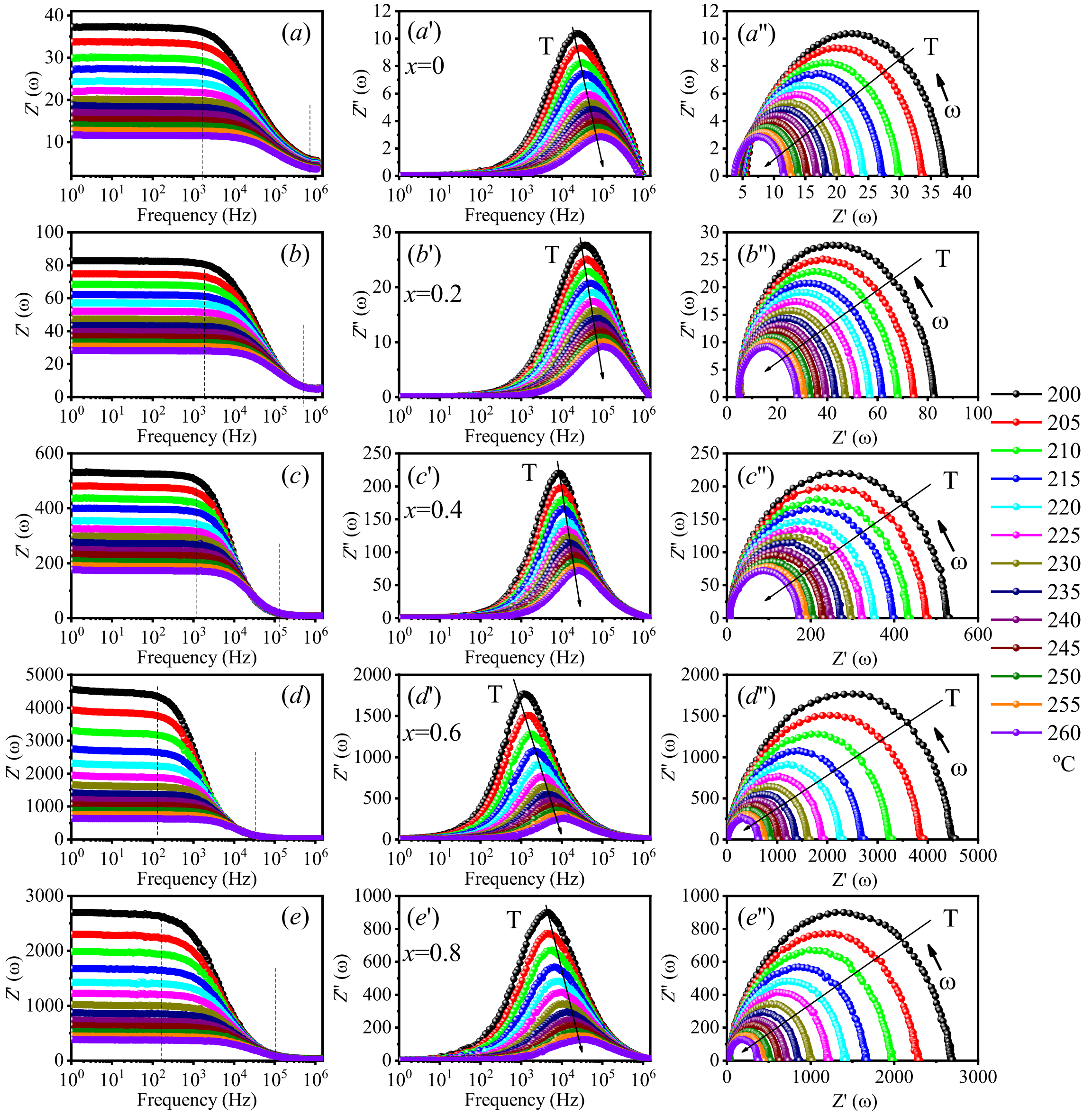

Fig. 9 Frequency dependence of the real $Z'(\omega)$, imaginary $Z''(\omega)$ parts, as well as Cole–Cole plots of the impedance spectra of samples (1-x) $PbFe_{12}O_{19}$–$x$$PbTiO_3$ $x=0.0$- (**a**), (**a′**), (**a″**), $x=0.2$- (**b**),(**b′**),(**b″**), $x=0.4$-(**c**),(**c′**),(**c″**), $x=0.6$- (**d**),(**d′**),(**d″**), $x=0.8$- (**e**),(**e′**),(**e″**)

curves, characteristic of relaxor behavior. The shift of the maxima is non-monotonic, and no distinct arcs corresponding to different phases, boundaries, and bulk grain regions are observed. Additionally, the Cole–Cole plots in Fig. 9(a'', b'', c'', d'', e'') do not highlight ferroelectric and magnetic phases or anomalies corresponding to the resistances of grain boundaries and volumes. The centers of the arcs are located above the $Z'(\omega)$ axis, indicating that the observed relaxation in these compositions is of the non-Debye type.

Using the experimental data for the relaxation time τ_m, we calculated the activation energies E_a of the compositions using the Arrhenius equation:

$$\tau_m = \tau_0 \exp(E_a/k_B T) \tag{7}$$

where τ_0 is the pre-exponential factor, E_a is the activation energy, k_B is Boltzmann's constant, and T is the absolute temperature.

As seen in Fig. 10(a), the plots of $\ln(\tau_m)$ versus inverse temperature for concentrations $x=0.0$ and 0.2, show kinks at about ~ 316 °C. The straight lines to the right of this temperature with energies of 0.36 and 0.49 eV correspond to the grain boundaries, while to the left they correspond to the bulk grains. For other concentrations (see Fig. 10(b)), the number of kinks with corresponding activation energies is higher, which may be due to

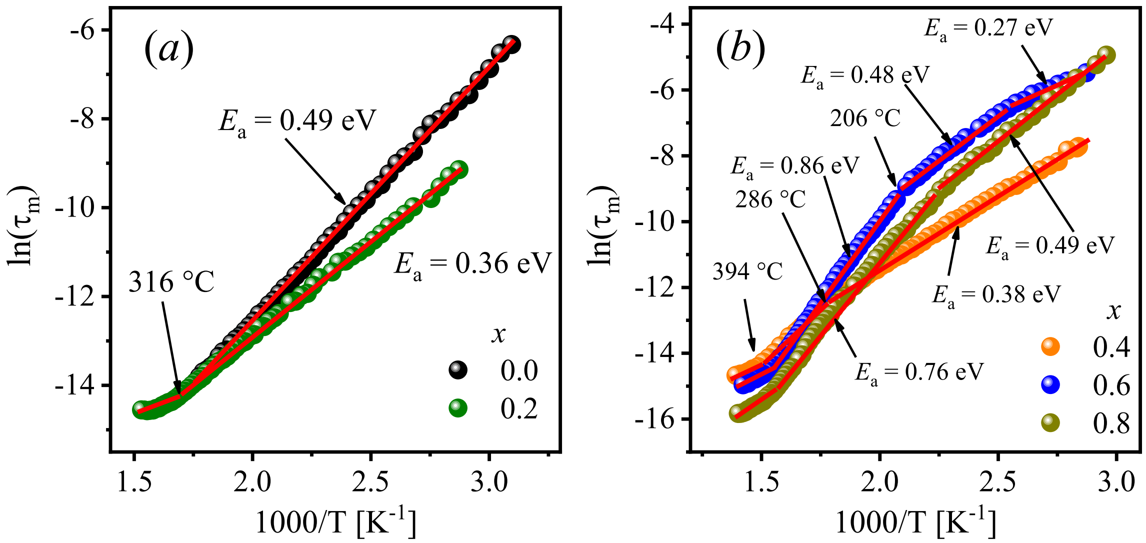

Fig. 10 Temperature dependencies of $\ln(\tau_m)$ for the compositions $(1\text{-}x)\mathrm{PbFe_{12}O_{19}} - x\mathrm{PbTiO_3}$: $x = 0.0$, 0.2 – (**a**), $x = 0.4$, 0.6, 0.8 – (**b**)

the increased concentration of the second phase in the composites, i.e., increased contributions to the conductivity from the boundaries and bulk grains of $\mathrm{PbTiO_3}$. The straight lines with energies of 0.27, 0.38, 0.48 and 0.49 eV also correspond to the grain boundaries of composites of corresponding concentrations. Energies of 0.76 and 0.86 eV correspond to bulk conductivity. The kinks observed to the left at 394 °C is close to 410 °C, as found earlier, and is most likely attributable to the magnetic component of the composite.

Figure 11(*a*, *b*, *c*, *d*, *e*) shows one experimental and theoretical $Z''(Z')$ curve obtained at $T = 150$ °C, along with the equivalent circuits derived using the EIS Spectrum Analyzer software package.

As shown in Fig. 11(*a*′), a noticeable kink is observed on the temperature dependence of the bulk grain resistance R_g around 150 °C, which is attributed to the discharge of charge accumulated at the grain boundaries. The grain boundary resistance R_{gb} also decreases with increasing temperature. From Fig. 11(a) it is evident that $\mathrm{PbFe_{12}O_{19}}$ is a highly conductive composition with bulk resistance of less than 30 ohms at 150 °C (see the small semicircle). The electrode resistances R_{el} have insignificant values, so they are not considered here. As the concentration of the ferroelectric component increases, the Z' of the composite increases, and the bulk and boundary components of the impedance are no longer distinguishable. The behavior of R_g and C_g for the remaining three compositions is similar (see Fig. 11 (*b*′, *c*′, *d*′, *e*′).

The bell-shaped maximum of C_g (CPE_g) in the temperature range $T = 150$–250 °C is due to Maxwell–Wagner polarization, and its further increase can be associated with the increased mobility of charge carriers trapped at the crystal lattice defects of the composite and the thermal expansion of the grain volume.

4 Conclusion

In this work, the structural state and physical properties of composites obtained from pre-synthesized and nanostructured powders and ceramics of $(1\text{-}x)\mathrm{PbFe_{12}O_{19}}$–$x\mathrm{PbTiO_3}$ have been studied. A comparative analysis of the physical properties of the initial compositions and those enriched with structural defects during the "top-down" nanostructuring process has been conducted. It was found that for the $\mathrm{PbTiO_3}$ component of the initial composition, a concentration point at $x = 0.4$ was observed, characterized by a minimum in D values and a sharp decrease in the unit cell parameters a^* and c^* of the mechanically activated compositions.

For the $\mathrm{PbFe_{12}O_{19}}$ component of a non-mechanically activated composition, a sharp leap in the unit cell parameters a and c is observed at $x = 0.2$, and D reaches a maximum at $x = 0.6$ and decreases by more than a half after mechanical activation. Depending on x, the values of the dislocation density ρ_D of the initial compositions of the $\mathrm{PbFe_{12}O_{19}}$ components exhibit a scatter in the range $(4.8–8.3) \times 10^{14}/\mathrm{m}^2$, and after mechanical activation, the ρ_D values increase by more than an order of magnitude and are in the range $(2.7–4.8) \times 10^{15}/\mathrm{m}^2$.

Using the FORC analysis method, the nature of the coercive field H_c and the interaction field dispersion depending on the concentration x and mechanical activation pressure have been studied. The magnetic phase transition temperature of composites depends significantly on the concentration x and the structural state, and it shifts to the left on

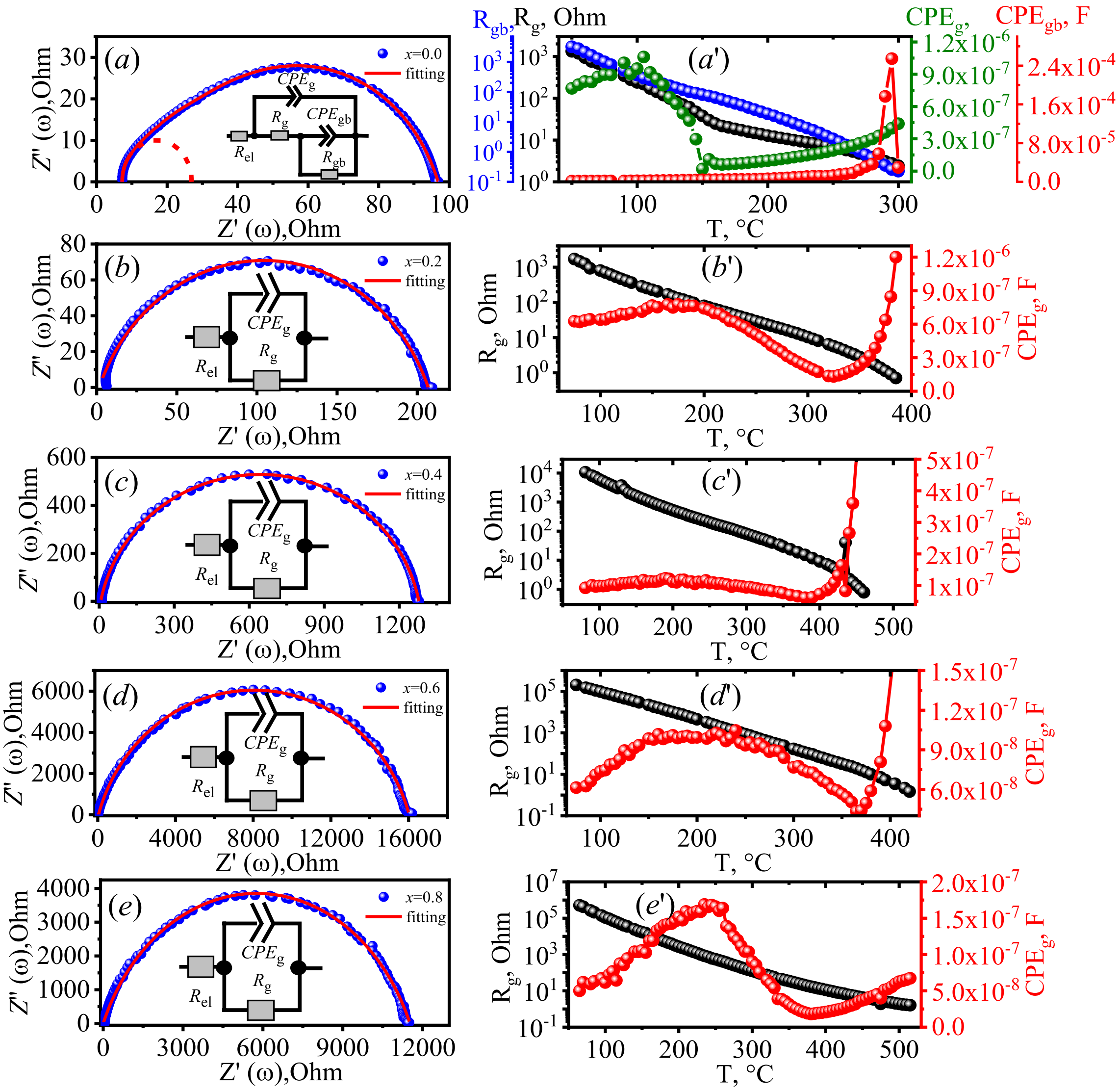

Fig. 11 Experimental and theoretical $Z''(Z')$ curves obtained at $T = 150$ °C and the equivalent circuits for the compositions $(1\text{-}x)\mathrm{PbFe_{12}O_{19}}$–$x\mathrm{PbTiO_3}$

the temperature scale after nanostructuring. Based on the study of the fundamental optical absorption edge of the composites, the E_g values have been calculated, and it has been found that nanostructuring of composites using the "top-down" method leads to an increase in E_g by approximately 0.3 eV.

The study of the relaxation properties of composites using impedance spectroscopy shows that with increasing x, the real part of the impedance $Z'(\omega)$ increases, and the temperature dependence of C_g exhibits a bell-shaped interval at $T = (150–350)$ °C, due to the Maxwell–Wagner relaxation.

Thus, it was shown that there is a correlated relationship between the concentration of structural defects formed during the mechanical activation of the $(1\text{-}x)\mathrm{PbFe_{12}O_{19}}$–$x\mathrm{PbTiO_3}$ composites and the concentrations of dopants on the one hand, and the parameters of the physical properties of the compositions on the other hand. The "top-down" nanostructuring method can be applied to vary the target physical properties of the composites within a wide range.

Supplementary Information The online version contains supplementary material available at https://doi.org/10.1007/s00339-024-08032-2.

Acknowledgements Research was financially supported by the Ministry of Science and Higher Education of the Russian Federation (State assignment in the field of scientific activity, No. FENW-2023-0019).

Author contributions All authors contributed equally to carrying out the present study. They wrote, read and approved the final manuscript.

Data availability Data will be available on request.

Declarations

Conflicts of interest The authors declare that they have no conflicts of interest.

References

1. R.C. Pullar, Prog. Mater. Sci. **57**, 1191 (2012)
2. D.I. Khomskii, J. Magn. Magn. Mater. **306**, 1 (2006)
3. W. Eerenstein, N.D. Mathur, J.F. Scott, Nature **442**, 759 (2006)
4. L. García-Cerda, J. Alloys Compd. **369**, 182 (2004)
5. V. Pankov, Mater. Sci. Eng. A **224**, 101 (1997)
6. S.E. Jacobo, L. Civale, M.A. Blesa, J. Magn. Magn. Mater. **260**, 37 (2003)
7. S.A. Oliver, M.L. Chen, I. Kozulin, C. Vittoria, J. Magn. Magn. Mater. **213**, 326 (2000)
8. B. E. Levin, Y. D. Tret'yakov, and L. M. Letyuk, (1979)
9. D. D. Mishin, (1981)
10. Y. M. Yakovlev and S. S. Gendelev, Moscow Sov. Radio **360**, (1975)
11. G.K. Thompson, B.J. Evans, J. Appl. Phys. **73**, 6295 (1993)
12. M. Pardavi-Horvath, J. Magn. Magn. Mater. **215–216**, 171 (2000)
13. F. Ansari, A. Sobhani, M. Salavati-Niasari, Compos. Part B Eng. **85**, 170 (2016)
14. V.G. Kostishyn, L.V. Panina, A.V. Timofeev, L.V. Kozhitov, A.N. Kovalev, A.K. Zyuzin, J. Magn. Magn. Mater. **400**, 327 (2016)
15. S. Prathap, W. Madhuri, Appl. Phys. A **125**, 314 (2019)
16. G. Nabiyouni, H. Halakoui, D. Ghanbari, J. Nanostructures **7**, 77 (2017)
17. B. Lahijani, K. Hedayati, M. Goodarzi, Main Gr. Met. Chem. **41**, 53 (2018)
18. E. Pollert, J. Hejtmaneck, J.P. Doumerc, J. Claverie, P. Hagenmuller, J. Phys. Chem. Solids **44**, 273 (1983)
19. H. Wang, Z.A. Li, M. Zhang, H. Tian, C. Zhu, Y. Zhang, H. Yang, J. Li, Phys. Status Solidi Basic Res. **256**, 1900157 (2019)
20. B.E. Watts, D. Regonini, F. Leccabue, F. Casoli, F. Albertini, G. Bocelli, D.S. Schmool, Mater. Sci. Forum **514–516**, 304 (2006)
21. O. Kubo, T. Ido, H. Yokoyama, IEEE Trans. Magn. **18**, 1122 (1982)
22. W. Zhong, W. Ding, N. Zhang, J. Hong, Q. Yan, Y. Du, J. Magn. Magn. Mater. **168**, 196 (1997)
23. N. Yang, H. Yang, J. Jia, X. Pang, J. Alloys Compd. **438**, 263 (2007)
24. G.-L. Tan, M. Wang, J. Electroceramics **26**, 170 (2011)
25. S.E. Mousavi Ghahfarokhi, Z.A. Rostami, I. Kazeminezhad, J. Magn. Magn. Mater. **399**, 130 (2016)
26. H.K. Choudhary, R. Kumar, A.V. Anupama, B. Sahoo, Ceram. Int. **44**, 8877 (2018)
27. S. Diaz, N. Suárez, J.C. Faloh, J.L. Sánchez, F. Leccabue, B.E. Watts, G. Albanese, Le J. Phys. IV **07**, C1 (1997)
28. S. Katlakunta, P. Raju, S.S. Meena, S. Srinath, R. Sandhya, P. Kuruva, S.R. Murthy, Phys. B Condens. Matter **448**, 323 (2014)
29. Y. Lin, N. Cai, J. Zhai, G. Liu, C.-W. Nan, Phys. Rev. B **72**, 012405 (2005)
30. K. Ban, M. Gomi, T. Shundo, N. Nishimura, IEEE Trans. Magn. **41**, 2793 (2005)
31. S. Díaz-Castañón, F. Leccabue, B.E. Watts, R. Yapp, J. Magn. Magn. Mater. **220**, 79 (2000)
32. A. L. Geiler, Y. He, S. D. Yoon, A. Yang, Y. Chen, V. G. Harris, and C. Vittoria, J. Appl. Phys. **101**, (2007)
33. S. Díaz-Castañón, F. Leccabue, B.E. Watts, R. Yapp, A. Asenjo, M. Vázquez, Mater. Lett. **47**, 356 (2001)
34. A.A. Bezlepkin, S.P. Kuntsevich, V.I. Kostyukov, Phys. Solid State **57**, 2213 (2015)
35. K. Abdulvakhidov, I. Dmitrenko, A. Soldatov, Z. Li, M. Sirota, Appl. Phys. A **128**, 88 (2022)
36. Z. Li, K. Abdulvakhidov, B. Abdulvakhidov, A. Soldatov, A. Nazarenko, P. Plyaka, A. Manukyan, V.J. Angadi, S. Shapovalova, M. Sirota, M. Vitchenko, I. Mardasova, E. Ubushaeva, S. Kallaev, Z. Omarov, Appl. Phys. A **128**, 1075 (2022)
37. K. Abdulvakhidov, Z. Li, B. Abdulvakhidov, A. Soldatov, S. Otajonov, R. Ergashev, D. Yuldashaliyev, B. Karimov, A. Nazarenko, P. Plyaka, S. Shapovalova, M. Vitchenko, I. Mardasova, E. Ubushaeva, E. Sitalo, Appl. Phys. A **129**, 185 (2023)
38. W. Kraus, G. Nolze, J. Appl. Crystallogr. **29**, 301 (1996)
39. V. T. Bublik and A. N. Dubrovina, Metall. Moscow (1978)
40. D.M. Vasil'ev, B.I. Smirnov, Sov. Phys. Uspekhi **4**, 226 (1961)
41. I.D. Mayergoyz, J. Appl. Phys. **57**, 3803 (1985)
42. R. Egli, Glob. Planet. Change **110**, 302 (2013)
43. Y. Yu, D.J. Dunlop, Ö. Özdemir, J. Geophys. **107**, EMP7 (2002)
44. C. Carvallo, A.R. Muxworthy, D.J. Dunlop, W. Williams, Earth Planet. Sci. Lett. **213**, 375 (2003)
45. G. Kortüm, W. Braun, G. Herzog, Angew. Chemie Int. Ed. English **2**, 333 (1963)
46. J. Tauc, R. Grigorovici, A. Vancu, Phys. Status Solidi **15**, 627 (1966)
47. F. Wooten, in *Opt. Prop. Solids*, edited by F. Wooten (Elsevier, 1972), pp. 42–84.
48. E.A. Davis, N.F. Mott, Philos. Mag. **22**, 0903 (1970)
49. K. Abdulvakhidov, A. Soldatov, I. Dmitrenko, Z. Li, S. Kallaev, Z. Omarov, Results Phys. **22**, 103905 (2021)